

Gyrokinetic electron acceleration in the force-free corona with anomalous resistivity

K. Arzner¹ and L. Vlahos²

¹ Paul Scherrer Institut, CH 5232 Villigen, Switzerland
e-mail: arzner@astro.phys.ethz.ch

² Department of Physics, Aristotle University of Thessaloniki, 54124 Thessaloniki, Greece
e-mail: vlahos@astro.auth.gr

Received 2. February 2006; accepted 27. March 2006

ABSTRACT

Aims. We numerically explore electron acceleration and coronal heating by dissipative electric fields.

Methods. Electrons are traced in linear force-free magnetic fields extrapolated from SOHO/MDI magnetograms, endowed with anomalous resistivity (η) in localized dissipation regions where the magnetic twist $\nabla \times \mathbf{b}$ exceeds a given threshold. Associated with $\eta > 0$ is a parallel electric field $\mathbf{E} = \eta \mathbf{j}$ which can accelerate runaway electrons. In order to gain observational predictions we inject electrons inside the dissipation regions and follow them for several seconds in real time.

Results. Precipitating electrons which leave the simulation system at height $z = 0$ are associated with hard X rays, and electrons which escape at height $z \sim 3 \cdot 10^4$ km are associated with normal-drifting type IIIs at the local plasma frequency. A third, trapped, population is related to gyrosynchrotron emission. Time profiles and spectra of all three emissions are calculated, and their dependence on the geometric model parameters and on η is explored. It is found that precipitation generally precedes escape by fractions of a second, and that the electrons perform many visits to the dissipation regions before leaving the simulation system. The electrons impacting $z = 0$ reach higher energies than the escaping ones, and non-Maxwellian tails are observed at energies above the largest potential drop across a single dissipation region. Impact maps at $z = 0$ show a tendency of the electrons to arrive at the borders of sunspots of one polarity.

Conclusions. Although the magnetograms used here belong to non-flaring times, so that the simulations refer to nanoflares and ‘quiescent’ coronal heating, it is conjectured that the same process, on a larger scale, is responsible for solar flares.

Key words. Acceleration of particles – Sun: corona, flares, X-rays, radio radiation – Methods: numerical

1. Introduction

Observations of radio waves and hard X-rays (HXR) from solar flares allow the study of the acceleration and propagation of high-energy electrons which are responsible for both types of emission. The picture emerging from the observations is generally complicated (Benz et al. 2005). While HXR (bremsstrahlung) emission is often associated with metric type III radio groups (Aschwanden et al. 1995), the timing of individual type III’s and HXR fine structure is erratic. Metric type III’s are presumably caused by electron beams exciting Langmuir waves, which then couple to electromagnetic (observable) modes. Sometimes, there is perfect agreement between type III onsets and HXR maxima, but in other cases there is no obvious peak-to-peak correlation, or one of the emissions is absent altogether. As a trend, the type III’s onsets were found to be delayed by fractions of a second against the HXR fine structures (Aschwanden et al. 1992; Arzner & Benz 2005a), although the type III frequency drift may assist such delays in

cases where the type III onset could not properly be resolved. At millimeter and decimeter wavelengths, synchrotron emission (e.g., Giménez et al. 2005), decimetric radio continuum and decimetric pulsations (Saint-Hilaire & Benz 2003), and decimetric spikes (Güdel et al. 1991) have also been found to be associated with HXR, roughly in the above decreasing order of association probability. These types of decimetric and millimetric radio emission are related to magnetically trapped electrons, where loss-cone instabilities are believed to be responsible for temporal structures (Kuijpers & Slotte 1976, Aschwanden & Benz 1988, Fleishman & Melnikov 1998).

The variety of observed behaviour accounts, on the one hand, for the non-linear (coherent) radio emission processes. On the other hand, it also reflects the geometric complexity of the active regions, which results from the nonlinear dynamics in the convection zone. In fact, the complex behaviour and the complex geometry are likely to be causes and effects of each other. Including a realistic amount of geometric complexity into a numerical model of solar flares was a major motivation for the present work.

Apart of geometrical aspects, the modeling of solar flares requires the specification of a physical acceleration mechanism. We shall assume here, as a working hypothesis, that acceleration is caused by DC parallel electric fields due to anomalous resistivity. Such fields are capable to accelerate high-energy electrons for which the electric force is no longer counterbalanced by the collisional drag (Dreicer 1960). It should be pointed out that runaway acceleration applies only to a small fraction of electrons in the high-energy tail of the electron distribution, and that the majority of electrons is (Joule) heated rather than accelerated to superthermal energies. The electric fields envisaged above are of macroscopic and dissipative nature, and mark the irreversible release of non-potential magnetic energy. We thus follow a scenario, proposed by Parker (1972,1983,1993), where the random photospheric footpoint motion twists and shears the coronal magnetic loops such as to develop tangential discontinuities. This happens intermittently and in multiple localized regions throughout the solar corona, and does not generally imply loop instability or global re-structuring of the solar corona. Parker's idea has initiated many investigations on coronal heating and -eruptions (e.g., Schumacher & Kliem 1996; Török & Kliem 2001; Gudiksen & Nordlund 2002), and has significantly improved the understanding of the global flaring process. In our view, a strong but heuristic argument for adopting dissipative (rather than conservative) electric fields as responsible for particle acceleration in solar flares is the intermittent and violent nature of flares, hinting to a catastrophic process which could not be cast in a Hamiltonian formalism. However, conservative electric fields, as used in most investigations on stochastic acceleration (e.g. Karimabadi et al. 1987; Schlickeiser 2003), may also act as particle accelerators.

In the present study, we adopt a test particle approach similar as in the simulations of Matthaeus & Lamkin (1986), Dmitruk et al. (2003, 2004), Arzner & Vlahos (2004), and Arzner et al. (2006), but with two important modifications. First, the electromagnetic force fields are not taken from MHD turbulence simulations or random-phase turbulence proxies, but from observed magnetograms. Secondly, in order to span the many orders of magnitude between the electron Larmor radius and the size of magnetic loops, we allow for gyrokinetic motion, keeping track of the gyro phase in an approximate way. This technique enables us to follow the electrons over several seconds in real time (several 10^8 gyro times), thus reaching the time scales on which solar flares are observed. In the simulations, runaway electrons are injected at $t = 0$ inside the localized dissipation regions, and followed numerically along (and sometimes across) the magnetic field lines. Observational predictions for HXR and radio waves are obtained as the electrons impinge the chromosphere, get trapped, or escape to the higher corona.

The article is organized as follows. Section 2 describes the construction of the coronal field; Section 3, the particle orbits; Section 4, the numerical results and observational predictions. These are then summarized and discussed in Section 5.

2. Coronal electromagnetic fields

Our domain is a slab of height H , bounded at $z = 0$ by the photosphere, and filled with time-independent force-free (e.g., Gary 1989) magnetic fields. We do not ask here for a perfect field reconstruction, but for a generic configuration which is compatible with the observation. Accordingly, we use an elementary linear force-free extrapolation from the normal photospheric magnetic field. This represents a local approximation at best (Wheatland 1999), and we have a slab thickness H of not more than a few 10^4 km in mind when fixing the physical scaling. (The linear force-free assumption predicts loops flaring with height, in contrast to the slender high-ranging loops observed by TRACE.) Further characteristic length and time scales are compiled in Table 1.

Symbol	Meaning	Typical value
Ω^{-1}	particle time unit	10^{-9} s
l_0	particle length unit	0.3 m
l	magnetogram resolution	660 km
L	magnetogram size	$1.7 \cdot 10^5$ km
H	slab height	$3 \cdot 10^4$ km
$1/\alpha$	force-free scale	$2 \cdot 10^4$ km
$1/u_c$	critical twist scale	$3 \cdot 10^3$ km

Table 1. Notation and physical scaling.

2.1. Construction of the force-free magnetic field

The force-free condition requires that $\nabla \times \mathbf{B} = \alpha \mathbf{B}$, where α is assumed to be constant ('linear' force-free field). Our construction of the force-free magnetic field follows the lines of Alissandrakis (1981), with modifications concerning the selection and number of Fourier modes. In order to avoid large but passive 3-dimensional arrays, the strategy is to locally compute $\mathbf{B}(\mathbf{x})$ from a restricted number of Fourier modes $\mathbf{b}(\mathbf{k}) e^{i\mathbf{k}\cdot\mathbf{x}}$. In terms of these, the force-free condition becomes $i\mathbf{k} \times \mathbf{b}(\mathbf{k}) = \alpha \mathbf{b}(\mathbf{k})$. This equation has a non-trivial solution only if $|\mathbf{k}|^2 = \alpha^2$, which we write in the form

$$k_z = \pm \sqrt{\alpha^2 - k_{\perp}^2} \quad \text{where} \quad k_{\perp}^2 = k_x^2 + k_y^2, \quad (1)$$

and if $\mathbf{b}(\mathbf{k})$ is proportional to

$$(-k_x k_z + i\alpha k_y, -k_y k_z - i\alpha k_x, k_x^2 + k_y^2). \quad (2)$$

See MacLeod (1995) for a deeper discussion of the curl eigenfunctions. We assume k_x and k_y to be real, so that the magnetic field in the (x, y) -plane is bounded, while k_z may be complex with positive imaginary part. Thus modes decaying or oscillating with height are permitted, and we shall use a small admixture of oscillating modes to transport structures from the chromosphere to larger heights. From a physics point of view this procedure is justified by noticing that the outstreaming solar wind (in a 1d slab geometry) does not require $\mathbf{B}(z)$ to vanish as $z \rightarrow \infty$. Furthermore, different wave vectors are not rational multiples of each other, so that the magnetic field extends

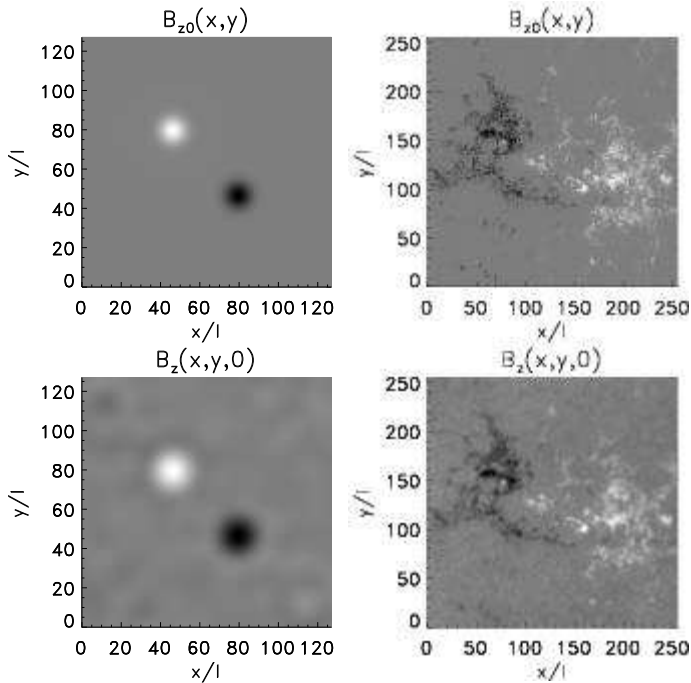


Fig. 1. Boundary fields (top) and their sparse-Fourier representations (bottom) of a bipolar configuration (left) and a SOHO/MDI magnetogram (right) recorded on August 17, 2002. 10:40 UT. The lower left corner of the magnetogram corresponds to $(78'', -36'')$ in heliocentric coordinates, and the scale is $l = 0.94''$.

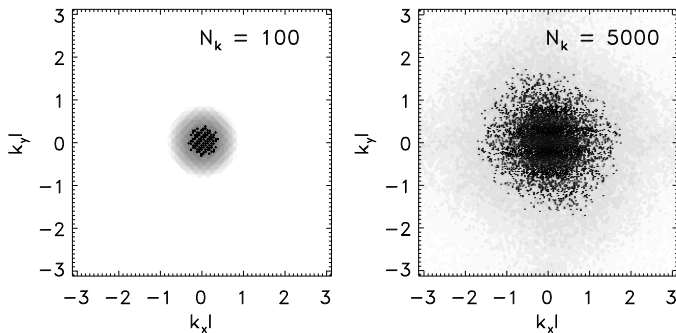


Fig. 2. Power spectral density (grayscale) of the boundary fields of Fig. 1 (top). Left: bipolar configuration; right: SOHO/MDI magnetogram. The sparse-Fourier components are marked by dots.

in a non-periodic, generic, way across the (x, y) -plane. The irregular spacing of the Fourier components also avoids aliasing artifacts, and their small number allows a non-expensive evaluation of the magnetic field even if no fast Fourier transform is available. However, the restriction to few Fourier components makes an exact matching of the boundary conditions impossible. Instead, we require agreement in a least square sense only, and minimize the mean-square deviation of the sparse-Fourier field $B_z(x, y, 0)$ and the photospheric boundary field $B_{z0}(x, y)$ in the square $L \times L$. Setting

$$\mathbf{B}(\mathbf{x}) = \text{Re} \sum_{\mathbf{k}} C_{\mathbf{k}} \mathbf{b}(\mathbf{k}) e^{i\mathbf{k} \cdot \mathbf{x}}, \quad (3)$$

normalizing the eigenvectors such that $|b_z| = 1$, and using the (approximate) orthogonality of the harmonic functions over $L \times L$, the coefficients $C(\mathbf{k})$ are given by

$$C(\mathbf{k}) \simeq \frac{\text{const.}}{N_k} \int_{L \times L} dx dy b_z^*(\mathbf{k}) e^{-i\mathbf{k} \cdot \mathbf{x}} B_{z0}(x, y). \quad (4)$$

The boundary field $B_{z0}(x, y)$ is given on a square lattice (cell size l^2), and the integral (4) is computed numerically. ‘Complementary’ solutions of the homogeneous boundary value problem (Chiu & Hilton 1977; Petrie & Lothian 2003) are disregarded. The sparse-Fourier wave vectors (k_x, k_y) are selected by the following procedure. First, the fast Fourier transform of the discrete boundary field is computed and those N_k (regularly spaced) wave vectors are chosen which have largest power spectral density. Then, a random perturbation $(\Delta k_x, \Delta k_y) \lesssim \pi/l$ is added in order to break the exact periodicity. The eigenvectors (Eq. 2) automatically ensure that $\nabla \cdot \mathbf{B} = 0$.

A test case with two Gaussian footpoints of opposite polarity is shown in Fig. 1 (left column), with the true boundary field $B_{z0}(x, y)$ presented in the top left panel and its sparse-Fourier version $B_z(x, y, 0)$ presented in the bottom left panel. The sparse-Fourier version contains $N_k = 100$ components only. This low number already provides a good approximation (correlation coefficient 0.94), because the Fourier spectrum (Fig. 2 left) is concentrated at the origin. When real data are used, a larger number of Fourier components is needed. This is illustrated in Figure 1 (right column), showing a SOHO/MDI magnetogram (top right) and its sparse-Fourier representation (bottom right) using 5000 Fourier components (Fig. 2 right). The magnetogram is located close to the center of the solar disc, so that projection effects are negligible. The magnetogram resolution is $l = 660$ km (rescaled from the original SOHO/MDI resolution), and the correlation coefficient between the magnetogram and its sparse-Fourier representation is 0.93. The magnetogram belongs to a non-flaring configuration and therefore the force-free extrapolation should be a reasonable approximation. Although the smallest scales are not well represented by the sparse-Fourier approximation, they rapidly decay with height (Eq. 1), so that the approximation becomes better as z increases. This fact is used to save computation time by restricting the field computation to components with $|e^{i\mathbf{k} \cdot \mathbf{z}}| > 10^{-3}$.

2.2. Properties of the magnetic field

Figure 3 displays the force-free magnetic fieldlines of the bipolar test case (top) and the SOHO/MDI magnetogram (bottom). The α parameter is such that $\alpha l = 0.03$, corresponding to a force-free scale $1/\alpha$ of about $2 \cdot 10^4$ km. The field lines start out at $z = 0$ at random with density proportional to $|\mathbf{B}|$. Several field line integration schemes have been tested, and the force-free condition was also verified using finite 3D differences. Most field lines connect the two poles of opposite polarity, but not all, because the sparse-Fourier field does not vanish outside the poles, nor outside $L \times L$.

The absolute scaling of \mathbf{B} is constrained by the SOHO/MDI data which give, for Figure 3 (bottom), a longitudinal photospheric rms field $\sqrt{\langle B_{z0}(x, y)^2 \rangle} = 50\text{G}$, with excursions to

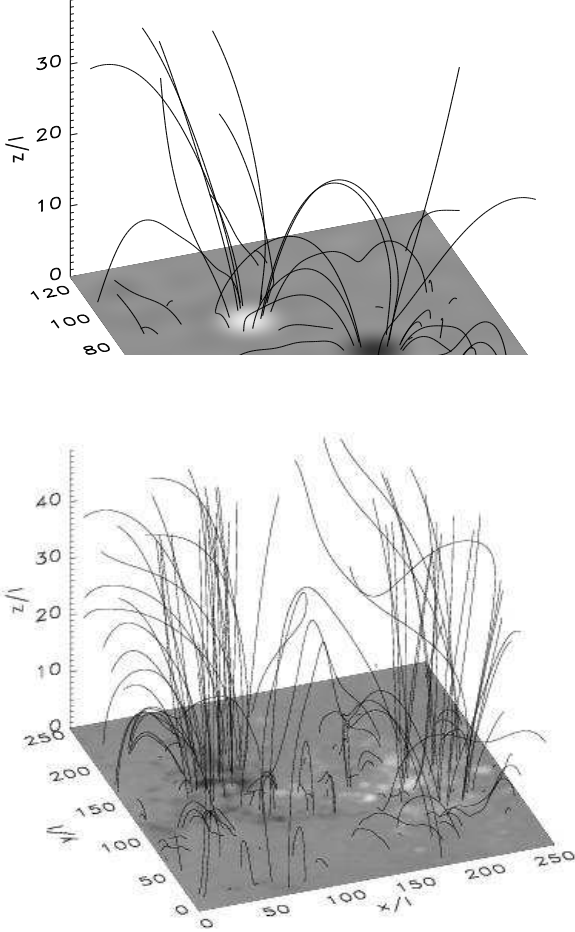


Fig. 3. Sparse-Fourier force-free magnetic field lines extrapolated from bipolar (top) and magnetogram (bottom) boundary data.

$\pm 400\text{G}$ at the footpoints. These values are typical for active regions; the average over the quiet solar surface is smaller ($\sim 1\text{G}$, see Kotov 2002). The mean-square magnetic field strength is related to the Fourier amplitudes by $\langle B_x(x, y, 0)^2 \rangle = \frac{1}{2} \sum_{\mathbf{k}} |b_x(\mathbf{k})|^2$ and similar relations for B_y and B_z .

2.3. Electric field

Since the configuration is assumed to be time-independent, the electric field has only an Ohmic component $\mathbf{E} = \eta \mathbf{j}$. The (scalar) resistivity η is either zero or anomalous, i.e., much larger than the collisional value η_{Spitzer} (Helander 2002). Regions with $\eta \gg \eta_{\text{Spitzer}}$ are called here ‘dissipation regions’. Owing to the force-free condition $\nabla \times \mathbf{B} = \alpha \mathbf{B}$, the electric field $\mathbf{E} = \eta \alpha \mathbf{B}$ is purely parallel.

Different criteria for the occurrence of anomalous resistivity have been proposed, relying on linear micro-instabilities or heuristic arguments. A well-known argument limits the electric current to $j_c = enc_s$ where c_s is the speed of sound (Papadopoulos 1980); an excess $|\nabla \times \mathbf{B}| > j_c$ is then argued to

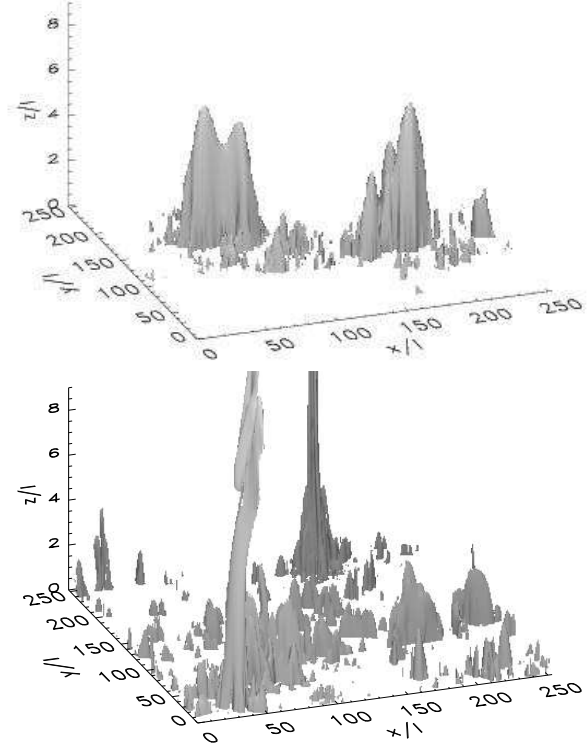


Fig. 4. Different definitions of dissipation regions. Top: current threshold. Bottom: magnetic twist threshold. Both panels refer to the magnetogram of Fig. 3 (bottom). It is the twist threshold which is used in the sequel of this paper.

produce shocks and dissipation in the current-carrying electron fluid. The resulting dissipation region $|\mathbf{j}| > j_c$ is depicted in Fig. 4 (top) for the configuration of Fig. 3 (bottom). As the force-free current is proportional to the magnetic field, the dissipation regions simply delineate the magnetic field strength.

Another approach invokes the twist or shear of magnetic field lines rather than the electric current density. The physical motivation for this stems from the observation that regions of larger magnetic field should also be able to guide larger currents before disruption. Thus the automatic increase of j_c with increasing $|\mathbf{B}|$ should be compensated, which is achieved by considering the quantity

$$\hat{\mathbf{b}} = \frac{\mathbf{B}}{|\mathbf{B}|} \quad (5)$$

rather than \mathbf{B} . The criterion for the occurrence of **anomalous** resistivity is then defined by

$$|\nabla \times \hat{\mathbf{b}}| < u_c. \quad (6)$$

The resulting dissipation regions are shown in Fig. 4 (bottom); the top and bottom panels represent equal dissipation volumes.

It follows from the force-free condition that $\hat{\mathbf{b}} \cdot \nabla \times \hat{\mathbf{b}} = \alpha$. Thus, for constant α , the field-aligned component of the magnetic twist $\nabla \times \hat{\mathbf{b}}$ is constant throughout the whole volume. This implies, in particular, that $|\nabla \times \hat{\mathbf{b}}|$ can never be smaller than α , and that the threshold u_c must be larger than α . In Fig. 4

(bottom), $u_c/\alpha = 6.6$. Since small scales with $k_\perp > \alpha$ decay exponentially with height, the steep gradients, and thus the dissipation regions, tend to accumulate at low altitudes. This is in agreement with the observation that the coronal heating function is localized within a height range $\lesssim 10^4$ km (Aschwanden 2001). The dissipation regions are thus not uniformly distributed in height, and the dissipative volume V_d can be characterized by a column height

$$h_d = V_d/L^2 \quad (7)$$

rather than by a volume fraction referring to the full numerical domain L^2H . In the case of Fig. 4 one has $h_d = 0.19l$.

The condition (6) is local. Non-local versions of Eq. (6) have been used by Georgoulis & Vlahos (1998) along pairs of magnetic field lines, and by Vlahos & Georgoulis (2004) on a discrete lattice. We use here Eq. (6), since it can be evaluated at the particle position and thus simplifies the simulation. The threshold u_c is chosen such that $u_c l = 0.2$.

3. Particle orbits

3.1. Dimensionless units and physical scaling

The system of units used in this article is similar as in Arzner & Vlahos (2004). Time is measured in units of Ω^{-1} where $\Omega^2 = \frac{1}{2} \sum_{\mathbf{k}} |\mathbf{b}(\mathbf{k})|^2$ is the non-relativistic mean-square gyro frequency at $z = 0$. Velocity is measured in units of the speed of light; energy is measured in units of mc^2 ; momentum is measured in units of mc ; distance is measured in units of $l_0 = c\Omega^{-1}$. We take $\langle |\mathbf{B}(x, y, 0)|^2 \rangle^{1/2} = 50\text{G}$ (see Sect. 2.2) to fix the absolute scaling, so that the electron cyclotron frequency is 140 MHz, the time unit is $\Omega^{-1} = 10^{-9}\text{s}$, and the length unit is $l_0 = 0.3\text{m}$. The electric field is measured in units of cB , and the resistivity η is measured in units of $c^2\Omega^{-1}$.

3.2. Exact orbits

In the above unit system, the exact particle equations of motion read

$$\frac{d\mathbf{x}}{dt} = \mathbf{v} \quad (8)$$

$$\gamma \frac{d\mathbf{v}}{dt} = \mathbf{v} \times \mathbf{B} + \mathbf{E} - (\mathbf{v} \cdot \mathbf{E})\mathbf{v} \quad (9)$$

where $\mathbf{E} = \eta \nabla \times \mathbf{B}$ and $\gamma = 1/\sqrt{1-v^2}$ is the Lorentz factor. Equations (8) and (9) are integrated by a traditional Cash-Karp/Runge-Kutta method (Press et al. 1998) with adaptive time step. The sparse-Fourier fields are computed at a lower rate, together with their Jacobians, from which a linear extrapolation to the actual particle position is made. The time step is chosen such that both the Cash-Karp error and the field extrapolation error remain within given bounds (Appendix A).

3.3. Gyrokinetic approximation

In the magnetic fields considered here, ranging from a few to a few hundred Gauss, and for typical kinetic energies between

1 keV and 1 MeV, the electron Larmor radius $\gamma v_\perp/\Omega$ varies from centimeters to hundreds of meters, and is therefore small compared to the resolution of the magnetic field ($l \sim 10^3$ km). The motion is thus almost always adiabatic, with possible exceptions at critical points of the magnetic field, and inside the dissipation regions. This suggests a gyrokinetic approximation, with the possibility to switch to exact orbits if necessary.

We base our guiding center mover on a relativistic (Brizard 1999) version of the gyrokinetic Equations of Littlejohn (1981, 1983). The variables considered are $(\mathbf{X}, p_\parallel, \Theta, \mu)$, where \mathbf{X} is the guiding center position, $p_\parallel = \gamma v_\parallel$ is the momentum parallel to the magnetic field, Θ is the gyro phase, and $\mu = \frac{1}{2} \gamma^2 v_\perp^2/B$ is the magnetic moment, which is a motion integral in the present approximation. The coordinates $(\mathbf{X}, p_\parallel)$ evolve according to

$$\frac{d\mathbf{X}}{dt} = \frac{1}{B_\parallel^*} \left(\frac{p_\parallel}{\gamma} \mathbf{B}^* + \frac{\mu}{\gamma} \hat{\mathbf{b}} \times \nabla B - \hat{\mathbf{b}} \times \mathbf{E}^* \right) \quad (10)$$

$$\frac{dp_\parallel}{dt} = -\frac{1}{B_\parallel^*} \mathbf{B}^* \cdot \left(\frac{\mu}{\gamma} \nabla B - \mathbf{E}^* \right) \quad (11)$$

where $\gamma = \sqrt{1 + p_\parallel^2 + 2\mu B}$ and

$$\mathbf{B}^* = \mathbf{B} + p_\parallel \nabla \times \hat{\mathbf{b}} \quad (12)$$

$$\mathbf{E}^* = \mathbf{E} - p_\parallel \frac{\partial \hat{\mathbf{b}}}{\partial t} \quad (13)$$

with $B_\parallel^* = \mathbf{B}^* \cdot \hat{\mathbf{b}}$. For our time-independent force-free magnetic field, \mathbf{E}^* equals \mathbf{E} and the last term in Eq. (10) vanishes.

In order to switch back to exact orbit integration we need to keep track of the gyro phase. In gyrokinetic approximations, the gyro phase is not unambiguously defined but subject to gauge freedom. Accordingly, various definitions have been proposed. We follow here Littlejohn (1988). Let $\hat{\mathbf{e}}$ be a unit vector in direction of the initial ($t=0$) Larmor radius. The vector $\hat{\mathbf{e}}_1$ is perpendicular to the direction $\hat{\mathbf{b}}$ of the local magnetic field, and a local cartesian triad is completed by setting $\hat{\mathbf{e}}_2 = \hat{\mathbf{e}}_1 \times \hat{\mathbf{b}}$. The task is to follow the unit vector $\hat{\mathbf{e}}_1$ along the gyro center, introducing a minimum of twist. This is achieved by solving the parallel transport (Fermi-Walker type) Equation

$$\frac{d\hat{\mathbf{e}}_1}{ds} = -\hat{\mathbf{b}} \left(\frac{d\hat{\mathbf{b}}}{ds} \cdot \hat{\mathbf{e}}_1 \right) \quad (14)$$

where s is the distance along the gyrocenter orbit. The gyro phase, with respect to the direction $\hat{\mathbf{e}}_1$, is then given by $\Theta = \int_0^t \gamma^{-1} |\mathbf{B}(\mathbf{X}(t'))| dt'$, and the exact orbit parameters (\mathbf{x}, \mathbf{v}) can be retrieved from $(\mathbf{X}, v_\parallel, \mu, \Theta, \hat{\mathbf{e}}_1)$. More details and the benchmarking of our numerical approach are described in Appendix A.

4. Simulation results and observational predictions

The slab-shaped simulation domain suggests a simple scheme of observational diagnostics, which is sketched in Figure 5. In this scheme, HXR are associated with electrons impacting $z =$

0, where they are stopped by the rapidly increasing density¹. Electrons which remain magnetically trapped are associated with gyrosynchrotron emission, and electrons which leave the simulation domain at $z = H$ are associated with radio type III emission at the local plasma frequency.

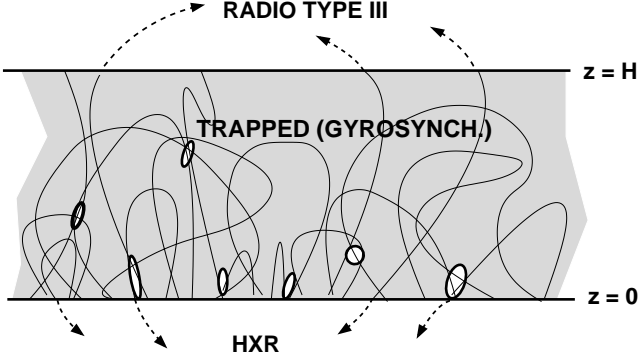


Fig. 5. Schematic allocation of different emissions from high-energy electrons. Precipitating electrons are associated with HXR; escaping and trapped electrons are associated with radio emission. Black lines symbolize magnetic field lines; boldface ellipses symbolize dissipation regions.

We have performed several simulation runs with varying parameters of the electromagnetic fields. One of these runs is discussed in detail in Sections 4.1 to 4.4, while the outcome of the others is summarized in Section 4.5. In all simulations, electrons with initial velocity $v_0 = 0.1c$ ($E_0 = 2.6$ keV) are injected at $t = 0$ inside the dissipation regions, and traced until one of the following conditions is met: $z < 0$ ('precipitation'), $z > H$ ('escape'), or $t > T_{\max}$ ('trapping'). The simulation duration T_{\max} is long compared to the average arrival times at $z = 0$ and $z = H$. T_{\max} is also long compared to the free escape time $\tau_0 \doteq H/v_0$ calculated on grounds of the initial velocity. The synchronized injection at $t = 0$ is somewhat artificial since we use magnetograms of a non-flaring active region. We have chosen this initial condition in order to model HXR and radio transients and thus provide additional (timing) diagnostics in situations where an observable flare pulse occurs, based on the assumption that flares are large-scale versions of the process considered here. The predictions will, though, be qualitative only, since the time evolution of the flaring region is not taken into account.

4.1. Electrons

The outcome of a typical simulation is summarized in Fig. 6. The top panel represents the exit rates at $z = 0$ and $z = H$. Most particles exit through the $z = 0$ boundary and the precipitation rate has a sharp peak at $\Omega t \sim 10^7$ (not resolved in Fig. 6). The escape rate peaks later. The remaining (trapped) population gradually decreases (Fig. 6 middle; times smaller than the

¹ Strictly speaking, $z = 0$ delineates the photosphere probed by the SOHO/MDI magnetogram, and not the density step (transition region) seen by the precipitating electrons. We shall not make this distinction here since our model does not include a background density profile.

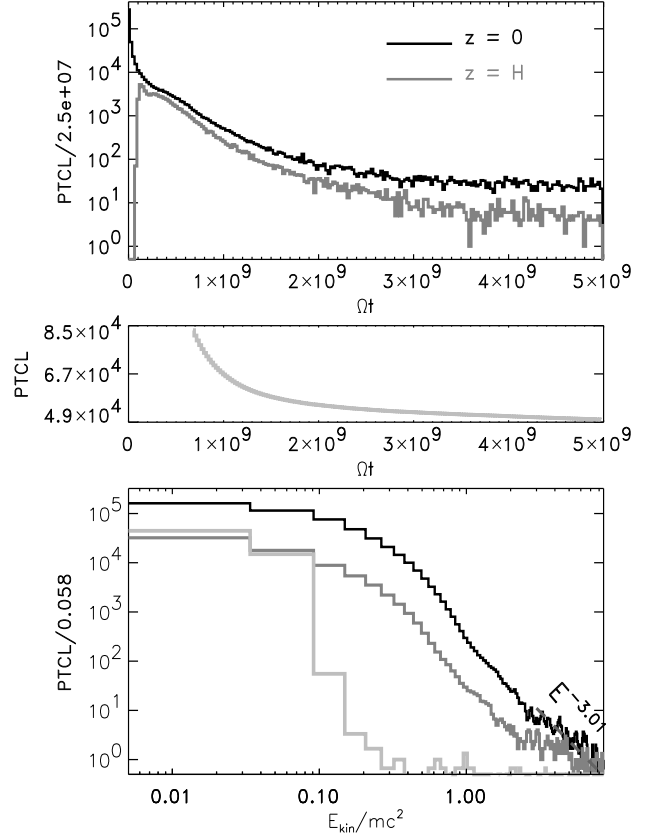


Fig. 6. Precipitating, escaping, and trapped electrons. Top: exit rates at the slab boundaries. Middle: remaining (trapped) particles. Bottom: terminal kinetic energies. $\Omega t = 5 \cdot 10^9$ corresponds to 5 seconds in real time.

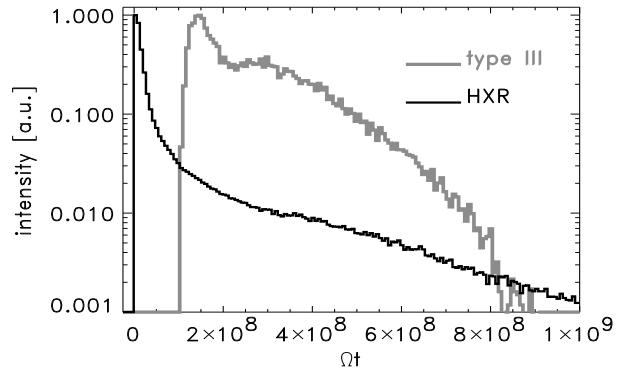


Fig. 7. Simulated HXR and type III light curves.

free escape time $\Omega\tau_0 = 6 \cdot 10^8$ are not shown). A detailed look on the particle orbits shows that these usually perform numerous visits to the dissipation regions before reaching relativistic energies. The fraction of time spent by the electrons inside the dissipation regions is quite different for the different populations. While precipitating particles spend about 10% of their time inside the dissipation regions, the escaping ones do so only for about 2%. The trapped ones spend 14% of their time inside the dissipation regions, but do not systematically gain energy.

In contrast, the escaping and – more pronounced – precipitating particles gain relativistic energies. The terminal energy spectra are shown in Fig. 6 (bottom). Non-Maxwellian tails occur in the precipitating spectrum at energies $E/mc^2 \sim 1$. The trapped electron spectrum (Fig. 6 light gray) refers to the end of the simulation ($t = T_{\max}$).

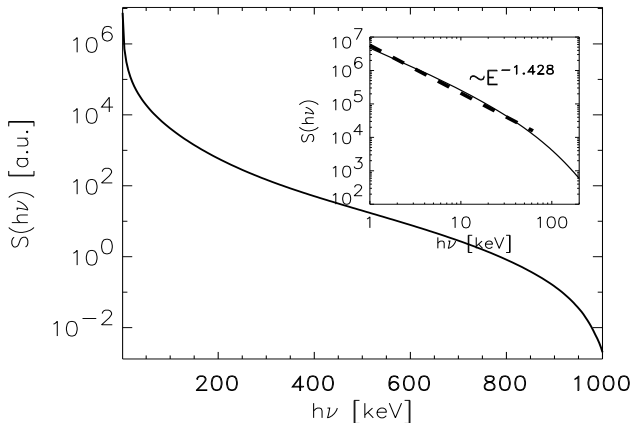


Fig. 8. Thick-target bremsstrahlung spectrum from the precipitating electrons.

4.2. Hard X rays

Light Curve and Spectrum. In our model, the precipitating population is associated with HXR bremsstrahlung, with the HXR time profile being directly proportional to the electron exit time density at $z = 0$ (Fig. 7). Since $z = 0$ is an absorbing boundary we use the thick-target approximation. The (orientation-averaged) bremsstrahlung cross section is taken from the fully relativistic formula 3BN of Koch & Motz (1959). The resulting HXR spectrum is shown in Figure 8. At energies up to ~ 40 keV, it can be fitted by a (hard) power law with index 1.4 (Fig. 8 inlet). At higher energies, it decays exponentially and finally drops off faster than exponentially at ~ 800 keV. Most of the exponential part and the super-exponential decay could usually not be observed with X-ray observatories like RHESSI because of the limited dynamic range (2-3 orders of magnitude for M class flares; see Grigis & Benz 2004).

Impact Map. The present simulation also predicts the sites at which electrons impinge onto the chromosphere (Fig. 9 left), and allows a comparison of this with the boundary magnetic field (Fig. 9 right, repeated here from Fig. 1 for better clarity). Since we inject particles in all dissipation regions simultaneously, the impact map represents a statistical prediction. There are two observations to be made: first, the electrons preferentially precipitate at negative magnetic polarity. Secondly, the impact density peaks not at the center of the sunspots or filaments, but at their borders. The first observation is a simple consequence of the constant- α assumption, by which the electric acceleration is always parallel or antiparallel to the mag-

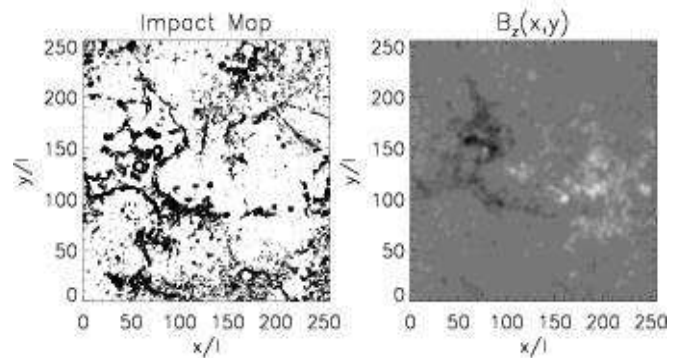


Fig. 9. Electron precipitation sites (left) and boundary magnetic field (right). Positive magnetic polarity is light; negative polarity is dark.

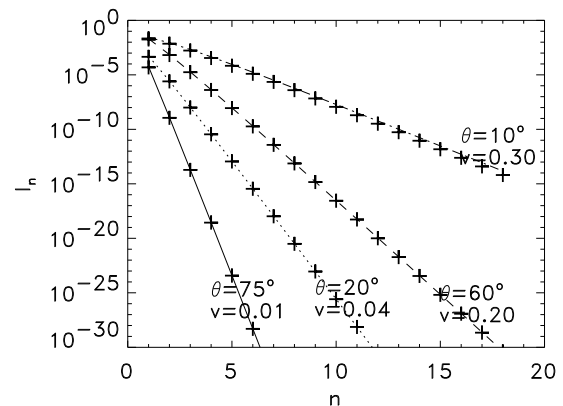


Fig. 10. Gyrosynchrotron intensity according to the exact expression (Eq. 15 – crosses) and its approximation (Eq. 16 – dotted line).

netic field². The second observation is a consequence of the mirroring in converging magnetic field lines, which makes it hard for electrons to penetrate down to $z = 0$ in regions of maximal $|\mathbf{B}(x, y, 0)|$. The actual impact map represents a trade-off between the number of downstreaming electrons and their reflection probability, which is optimal at the sunspot/filament boundaries.

4.3. Electron beams

Electrons which escape to altitudes $z > H$ are considered as a proxy for type III radio bursts. Contrary to the incoherent bremsstrahlung and gyrosynchrotron radiation, the plasma emission of type III bursts is coherent and therefore not proportional to the number of emitting electrons. The non-linear dependence (say, $\propto N^\xi$ with $\xi > 1$) compensates for the relatively tenuous escaping population. The resulting time signal is shown in Fig. 7, together with the HXR light curve. The scaling of the two intensities is arbitrary. As the background plasma density is not specified in our model, we cannot pre-

² We have assumed here positive α and that the electrons have positive charge.

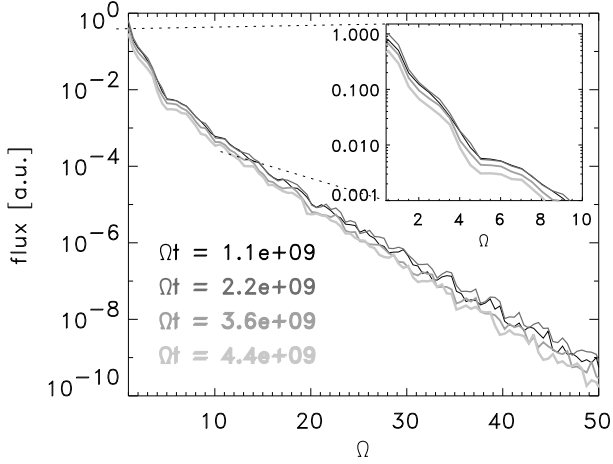


Fig. 11. Optically thin gyrosynchrotron spectrum emitted in z direction. Different curves represent different times. $\Omega = 1$ corresponds to about 1 GHz.

dict the emission frequency of the plasma waves. However, we may consult observed density profiles at height $H \sim 3 \cdot 10^4$ km, yielding $n_e \sim 2.5 \cdot 10^8 \text{ cm}^{-3}$ averaged over the quiet corona (Fludra 1999). This number varies by a factor 3 when equator-to-pole variation is taken into account (Gallagher et al. 1999), and may be larger by a factor 10 above faculae (Dumont et al. 1982). Thus we associate a plasma density of 10^8 cm^{-3} to $2 \cdot 10^9 \text{ cm}^{-3}$ with the $z = H$ boundary of our simulation slab, corresponding to a plasma frequency of 100 to 400 MHz.

4.4. Gyrosynchrotron emission

The electrons which are trapped in closed loops are thought to be responsible for gyrosynchrotron radiation, manifesting in microwave solar continuum bursts³. In this case there are many bursts which are optically thin at all frequencies (Fleishman et al. 2003), and we assume here optically thin radiation for simplicity. Moreover, we neglect the plasma response and consider emission in vacuum. Therefore, our results apply to the emission at frequencies above the spectral peak provided by either optical thickness or the Razin effect. An electron on a circular orbit emits then at frequency $n\omega/\gamma$ the intensity (Schott, 1912)

$$I_n = \frac{n^2 \omega^2}{\gamma^2} \left(\tan^2 \theta J_n^2(nv \cos \theta) + v^2 J_n^2(nv \sin \theta) \right) \quad (15)$$

where n is an integer, $\omega = eB/m$ is the local cyclotron frequency, and θ is the angle between the gyration plane and the line of sight, which latter is taken along the z -direction. In our simulation, most trapped electrons have velocities $v \ll 1$ (Fig. 6 bottom), so that the argument of the Bessel functions in Eq. (15) is small and $J_n(z)$ can be approximated by $(2\pi n)^{-1/2} (ez/2)^n$ (Abramowitz & Stegun, 1970), yielding

$$I_n \simeq \frac{\omega^2}{\gamma^2} \frac{1 + \sin^2 \theta}{\cos^2 \theta} \frac{n}{2\pi} \left| \frac{ev \cos \theta}{2} \right|^{2n}, \quad (16)$$

³ In contrast, narrowband decimetric continua are better explained by transition radiation (Fleishman et al. 2005, Nita et al. 2005).

where Euler's number $e = 2.718$ is not to be confused with the elementary charge. The relative accuracy of the approximation (16) is of order $|v \cos \theta|$ for all n ; a numerical illustration is shown in Fig. 10. From Eq. (16) we see that the intensity I_n decays exponentially with n , so that the radiation is concentrated at low harmonics. In the limits $v \rightarrow 0$ and $\theta \rightarrow 90^\circ$ only the fundamental ($n = 1$) contributes. If the velocity has a component parallel to the magnetic field and to the observing direction, this results in a Doppler shift $\omega \rightarrow \omega^*$, and v in Eqns. (15, 16) has to be replaced by v_\perp , the component perpendicular to the magnetic field. Neglecting dispersion and absorption, we may thus obtain the radio spectrum by accumulating a histogram of the frequencies $n\omega^*/\gamma$ with weight I_n for all particles and times. The result is shown in Figure 11. Note that the spectrum decays monotonically and approximately exponentially with frequency, which is different from the familiar synchrotron ($\gamma \gg 1$) shape with powerlaw rise and -decay. Here, the exponential decay is mostly caused by the harmonics dependence (Eq. 16) but also supported by the exponential decay of magnetic field with height. Individual harmonics are washed out because of the magnetic field inhomogeneity.

run	N_k	N_x	l [km]	H/l	αl	η [c^2/Ω]	h_d/l
1)	5000	128	875	40	0.05	4.38	0.56
2)	5000	256	660	50	0.05	6.84	0.50
3)	5000	256	660	50	0.03	6.84	0.19
4)	5000	256	660	64	0.01	6.84	0.13
5)	1000	256	660	64	0.01	6.84	0.05
6)	1000	256	660	64	0.01	1.37	0.08

Table 2. Simulation parameters. In all simulations, $\Omega^{-1} = 10^{-9}$ s and $u_c l = 0.2$.

4.5. Parameter exploration

We have performed various production runs, involving a total CPU time of about 4 months. Different runs have different values of the parameters H (slab height), α (force-free parameter), and η ; see Table 2. The critical twist is fixed at $u_c l = 0.2$. The simulation discussed in Sections 4.1 - 4.4 is labeled 3 and represents an intermediate case. Each simulation involves several 10^5 particles. An overview on the simulation results is presented in Fig. 12. The column a) contains the electron exit rates at $z = 0$ (black line) and $z = H$ (gray line) during the first third of the simulation time, normalized by the total number of simulated electrons. The column b) shows the energy distributions at the end of the simulation ($t = \text{exit time}$, or $t = T_{\text{max}}$). The translation of the electron results onto HXR and radio wave predictions proceeds similar as in Sections 4.2 to 4.4, and preserves the hardness ordering of the spectra.

The simulations 1 to 6 may be summarized by saying that the results of Sections 4.1 to 4.4 are generic, in the sense that the general shape and relative timing of the light curves are robust against variation of (H, α, η) . However, the time scaling, the division into precipitating and escaping populations, and the spectrum depend on the parameters (Tab. 2). The time

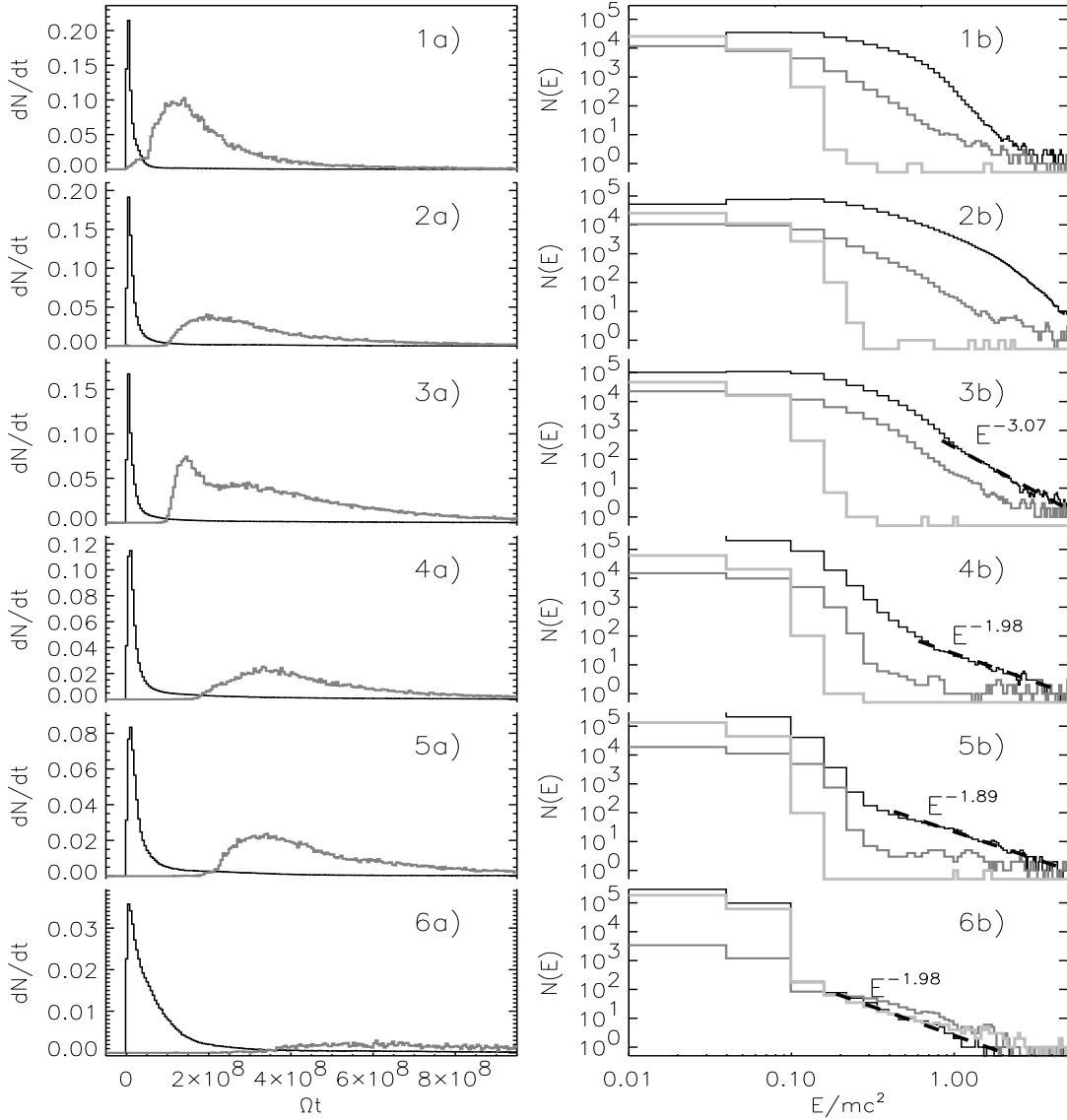


Fig. 12. Parameter exploration. Left column: exit rates. Right column: terminal energy spectra. Black (gray, light gray) lines refers to precipitating (escaping, trapped) populations. See Tab. 2 for the simulation parameters.

delay between the precipitation pulse and the onset of escape (Fig. 12 left) increases, naturally, with the slab height H . It also depends on the force-free parameter α , yet in a more subtle way. From the comparison of simulations 2 and 3 it is seen that a larger α favours prompt escape. This is not immediately obvious, since a larger α implies a smaller force-free scale $1/\alpha$ and thus smaller magnetic loops which do not protrude to $z = H$. However, a larger α also admits more non-decaying modes ($k_{\perp} < \alpha$) and thus more open field lines along which the electrons can escape. Moreover, a larger α implies larger curvature, so that the criticality condition (Eq. 6) is more frequently met and the accelerating volume is larger ($h_d = 0.5l$ in simulation 2 but $h_d = 0.19l$ in simulation 3). As a net effect, a large force-free parameter α thus favours rapid acceleration and escape. A similar enhancement of acceleration by the presence of small scales accounts for the difference between panels 4 and 5 in Fig. 12. These simulations differ only by the number of Fourier

components. Run 4 contains wave vectors up to $k_{\perp}l \leq 1.94$, whereas run 5 contains wavevectors $k_{\perp}l \leq 0.8$. Accordingly, run 4 reaches somewhat higher energies (panels 4b and 5b). The escape time also increases (and the escape probability decreases) with decreasing anomalous resistivity and thus with decreasing electric field (5a vs. 6a). The trapped component (light gray) is throughout softest, except for the case of very small resistivity (run 6) where all 3 populations behave similarly for $E/mc^2 \gtrsim 0.1$. Run 6 is similar to run 5 but with smaller resistivity, compensated by a somewhat larger dissipation volume.

As a general trend, it can be seen from Fig. 12 (top to bottom) that smaller dissipation volumes and weaker electric fields yield a more gradual evolution and less intermediate energies ($0.1 < E/mc^2 < 1$) but a comparable amount of high energies, so that the energy histograms have more tenuous but harder tails. This reflects a change of the nature of acceleration from

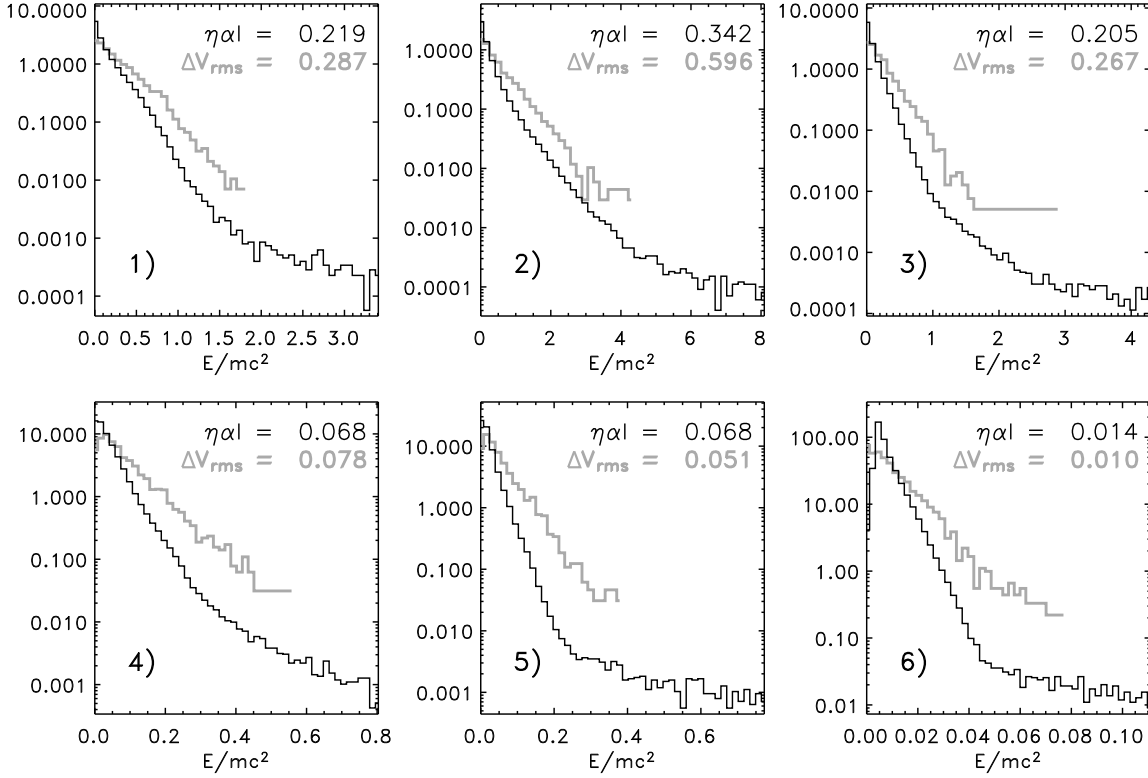


Fig. 13. The distribution of precipitating, escaping, plus trapped particle energy (black line) and the distribution of voltage drops (gray line).

frequent and small energy increments to rare but violent energy gains, in the course of which the stochastic process leaves the domain of attraction of the central limit theorem.

5. Summary and Discussion

We have simulated gyrokinetic electron orbits in constant- α force-free magnetic fields with anomalous resistivity η . The latter is localized in (postulated) dissipation regions where the magnetic twist $\nabla \times \hat{\mathbf{b}}$ exceeds a given threshold u_c , corresponding to a critical scale $1/u_c \sim 3000$ km. The dissipation regions cover about 10^{-3} of the simulated slab volume, and can be characterized by a column height h_d of 30 to 300 km. The (parallel) dissipative electric field exceeds the Dreicer field by one or two orders of magnitude and yields direct acceleration of runaway electrons. In general, the electrons visit numerous dissipation regions before reaching relativistic energies, and arrive at the chromosphere before escaping to the higher corona. The latter ordering agrees with an observed trend for HXR to precede type III bursts (Aschwanden et al. 1992; Arzner & Benz 2005a), also in terms of absolute time delays.

From a physics point of view, one may compare the energies reached in Fig. 12 to the voltage drop along the magnetic field line inside a (simply connected) dissipation region \mathcal{D} . (We use here the term ‘voltage drop’ rather than ‘potential drop’ since $\mathbf{E} = \eta \mathbf{j}$ is not a potential field.) The quantity $\Delta V = \int_{\mathcal{D}} \mathbf{E} \cdot d\mathbf{l}$ gives an upper limit on the energy which can be gained inside a single dissipation region; reflection from converging field lines (and also deceleration from \mathbf{E} itself) does

generally prevent the particles from exploiting the full voltage drop. By choosing $5 \cdot 10^3$ random points inside the dissipation regions, and following the magnetic field lines going through these points, we find the distribution of voltage drops shown in Fig. 13 (gray line), together with the distribution of all terminal electron energies (black line). Both kinetic energy and voltage drops are measured in units of the electron rest mass. As can be seen, the two distributions scale similarly in energy from one simulation to another (note the different energy axes!), and the sub-exponential tails of the particle energy occur above the largest voltage drop present in the simulation. This agrees with the observation that many dissipation regions are visited before the particles reach the highest energies. The root mean square voltage drops ΔV_{rms} are of the order of the voltage drop across the magnetogram resolution, $\eta \alpha l$. The distribution of voltage drops decays slower than the distribution of particle energies, which relates to the fact that ΔV_{rms} is merely an upper bound on the kinetic energy gain. The peak of the particle distributions at lowest energies is mostly due to the trapped component.

The present model predicts a statistical preference for the HXR to occur at one magnetic polarity, because of the assumption of constant α , by which the electric field $\mathbf{E} = \eta \alpha \mathbf{B}$ is always parallel ($\alpha > 0$) or antiparallel ($\alpha < 0$) to the magnetic field. The electrons preferentially impact the chromosphere not in the center of sunspots or filaments (where $|\mathbf{B}|$ is largest) but at their borders. Ions, due to their opposite charge, should preferentially impact at opposed magnetic polarity (but the ion dynamics is not directly comparable to the electron dy-

namics because of the large mass ratio). The experimental verification or falsification of this model prediction, using non-randomized force-free extrapolations and spatially resolved X-ray (e.g., RHESSI) observations of flaring active regions, will be the subject of future investigations. It should also be pointed out that the impact map (Fig. 9) is obtained from simultaneous injection in all dissipation regions. If injection was restricted to a single dissipation region or group of dissipation regions, then only few impact regions would occur, as usually observed in individual solar flares.

Finally, we should mention that the present approach has many caveats. Most prominent among them is the fact that test particle simulations can not tell us anything about the absolute number of electrons which are accelerated, and their application to the real solar corona requires caution in order to match global electrodynamic constraints (i.e. return currents; Spicer & Sudan 1984). As a rule, our simulations can only account for a tenuous high-energy tail, because the back-action on the electromagnetic field and Coulomb collisions are neglected. Then, we have used here magnetograms of non-flaring active regions – where the force-free extrapolation should be a good approximation – and have thus envisaged ‘quiescent’ coronal heating by nanoflares rather than large isolated events. The observable predictions, though, address sizable flares where all types of emission can be detected. We suggest that the actual flares are generated by a similar process, and should thus have similar characteristics. Conversely, the non-flaring active regions are constantly doing what flaring active regions do but in smaller, possibly undetected numbers. This coronal process may account for spatial X-ray and radio fine structures in quiet solar regions (Benz et al. 1997) and non-thermal electrons measured in space during quiet times (‘superhalo’; Lin 1998), as an alternative explanation of MHD wave acceleration in the solar wind. Also, the assumption of a time-independent magnetic field is an approximation only. It is certainly violated during large flares with re-structuring of the global magnetic topology. Also, it does not formally account for the continuous footpoint motion driving the Parker (1983) scenario. However, it may be a reasonable approximation for medium-size flares, where the Parker mechanism does not destroy the overall magnetic field structure. This point of view is supported by the work of Aulanier et al. (2005a, 2005b) who numerically study the evolution of magnetic flux tubes and quadrupolar configurations under sub-Alfvénic photospheric motion. Their (incompressible, resistive) MHD simulations demonstrate that current sheet formation and topological changes may be described by a sequence of quasi-equilibria, so that a static approximation over a few ten seconds seems appropriate. With regard to particle acceleration, the temporal evolution of the magnetic fields is expected to decrease trapping and facilitate both precipitation and escape.

Acknowledgements. The authors thank Emmanuela Rantsiou and Manolis Georgoulis for help with SOHO/MDI magnetograms, and Arnold Benz and Gregory Fleishman for helpful discussions and comments. This work was supported in part by the Research Training Network (RTN) ‘Theory, Observation and Simulation of Turbulence in Space Plasmas’, funded by the European Commission (contract No. HPRN-eT-2001-00310).

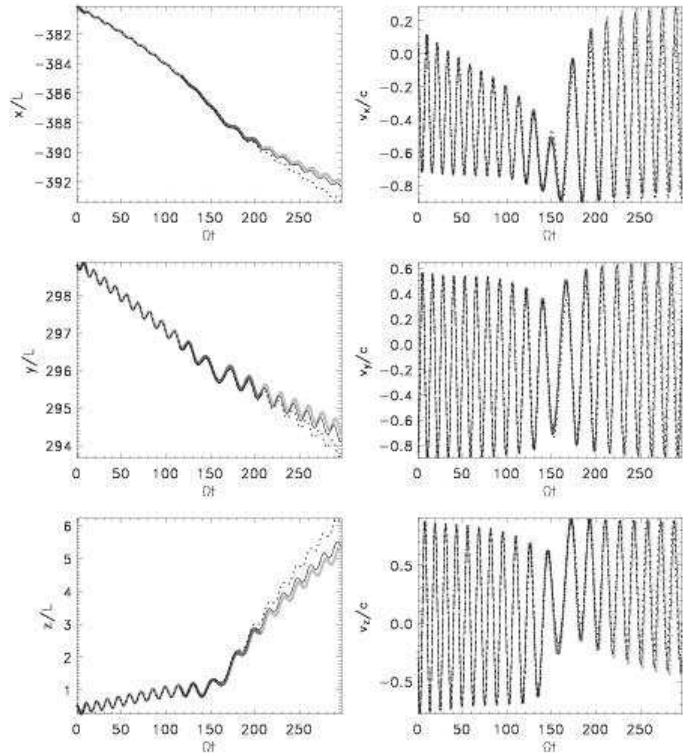


Fig. 14. Benchmark of the orbit integration schemes, showing position (left column) and velocity (right column) of a relativistic electron in strongly curved ($l/l_0=10$) magnetic fields. Solid line represents exact orbits (Eqns. 8,9); dotted line, gyrokinetic approximation (Eqns. 10 - 14). Gray crosses represent the hybrid mode, with the exact regime marked dark and the gyrokinetic regime marked light.

Appendix A: Numerical Implementation

A.1. Regime switching and accuracy control

The choice of the orbit integration method, exact or gyrokinetic, depends on two constraints. From a physical point of view, the gyrokinetic approximation requires the Larmor radius to be small compared to the scale of the magnetic field, $\rho \ll l$. From a numerical point of view, the gyrokinetic approximation is faster than exact orbit integration whenever the latter is dominated by particle motion rather than by field evaluation. Indeed, if τ_f denotes the CPU time needed for a single field evaluation and τ_g is the CPU time needed to resolve a single gyration, then the gyrokinetic approximation is by a factor

$$f = \frac{\tau_g}{\tau_f} \times \frac{l}{\rho} \quad (\text{A.1})$$

faster than exact orbit tracking. The time τ_g is approximately independent of the integration scheme as long as this is optimal, and a typical value on a medium-size workstation is found to be $\tau_g \sim 5 \cdot 10^{-5} \text{ s}$. The time cost of a single field evaluation, on the same hardware, is $\tau_f \sim N_k \times 5 \cdot 10^{-6} \text{ s}$ with N_k the number of Fourier components. Therefore the gyrokinetic method is numerically beneficial for $N_k < 10 \times l/\rho$. Thus, if

the gyrokinetic approximation is physically allowed ($l/\rho \gg 1$) then it is also numerically beneficial in the sparse-Fourier representation; the upper bound on N_k is in practice rarely met.

We turn now to the precise (and implemented) formulation of regime switching and accuracy control. The gyrokinetic approximation requires that the magnetic field should change slowly across a Larmor radius, $(\nabla \mathbf{B}) \cdot \boldsymbol{\rho} < \epsilon_g B$, where $\nabla \mathbf{B}$ is the Jacobian and $\epsilon_g \ll 1$. For practical purposes, we replace this by the stronger and computationally less expensive constraint $\rho^2 \sum_{ij} |\partial_i B_j|^2 < \epsilon_g^2 B^2$ with $\rho = |\mathbf{p}|/B$. The quantity ρ also includes parallel momentum, so that the condition accounts for particle acceleration inside the dissipation regions. In addition to the gyrokinetic approximation error, there are numerical errors from the finite time step and field computation rate. These are controlled by limiting the Cash-Karp position- and momentum errors, and by enforcing re-calculation of the electromagnetic fields if $|\Delta \mathbf{x}|^2 \sum_{ij} |\partial_i B_j|^2 > \epsilon_B^2$, where $\Delta \mathbf{x} = \mathbf{x} - \mathbf{x}_{old}$ is the distance to the last field evaluation point \mathbf{x}_{old} . Using the same Jacobian, the fields are linearly extrapolated from \mathbf{x}_{old} . In order to avoid relentless switching between exact and gyrokinetic regimes, a minimum duration of one gyro period in each of the regimes is enforced.

A.2. Benchmarks

The exact orbits have been computed with different integration- and field evaluation schemes. The time integrators include the Verlet scheme and other leapfrog variants, and Runge-Kutta schemes with and without adaptive time stepping. The field evaluation was done either pointwise or with linear interpolation involving $\nabla \mathbf{B}$. Once the exact orbits were established, they have been used to benchmark the gyrokinetic orbits. As an example, Figure 14 displays individual cartesian components of position and velocity in an extreme situation, i.e. for a highly relativistic ($v = 0.99c$) particle with small magnetic scales ($l/l_0 = 10$). Solid line represents exact orbits, dotted line represents the gyrokinetic approximation, and gray represents the hybrid mode with automatic regime switching, where exact (gyrokinetic) regimes are marked dark (light). In the hybrid method, the particle starts with exact orbit integration and switches to the gyrokinetic description at $\Omega t \sim 10$. It remains then in the gyrokinetic mode until at $\Omega t \sim 120$ a region of strong magnetic curvature is encountered, where exact orbit tracing is enforced (dark gray). At $\Omega t \sim 200$ the orbit switches back to the gyrokinetic method (light gray). During the gyrokinetic phase, the magnetic moment is conserved to within 0.1%, but varies during the exact-orbit phase by some 80%. As can be seen, the hybrid orbit is closer to the exact result than the purely gyrokinetic orbit.

References

- Abramowitz, M., and Stegun, I., 1970, Handbook of mathematical functions, 7th ed., Dover Publ. Inc., New York
- Amari, T., Aly, J. J., Luciani, J. F., Boulmezaoud, T. Z., & Mikic, Z., 1997, *Solar Phys.*, 174, 129-149
- Alissandrakis, C. E., 1981, *A&A*, 100, 197
- Arzner, K., & Vlahos, L., 2004, *ApJ*, 605, L69
- Arzner, K., & Benz, A., 2005, *Solar Phys.*, 231, 117-141
- Arzner, K., Knaepen, B., Carati, D., Denewet, N., & Vlahos, L., 2006, *ApJ*, 637, 322-332
- Aschwanden, M., & Benz, A. O., 1988, *ApJ*, 332, 447
- Aschwanden, M. J., & Güdel, M., 1992, *ApJ*, 401, 736
- Aschwanden, M. J., Montello, M. L., Dennis, B. R., & Benz, A. O., 1995, *ApJ*, 440, 394
- Aschwanden, M. J., 2001, *ApJ*, 560, 1035-1044
- Aulanier, G., Démoulin, P., & Grapin, R., 2005, *A&A*, 430, 1067-1087
- Aulanier, G., Parlat, E., & Démoulin, P., 2005, *A&A*, 444, 961-976
- Benz, A. O., Krucker, S., Acton, L. W., & Bastian, T., 1997, *A&A*, 320, 993-1000
- Benz, A. O., Grigis, P. C., Csillaghy, A., & Saint-Hilaire, P., 2005, *Solar Phys.*, 226, 121-142
- Brizard, A. J., and Chan, A. A., 1999, *Phys. Plasmas*, 6, 4548
- Chiu, Y. T., & Hilton, H. H., 1977, *ApJ*, 212, 873-885
- Dmitruk, P., Matthaeus, W. H., Seenu, N., & Brown, M. R., 2003, *ApJ*, 597, L81
- Dmitruk, P., Matthaeus, W. H., & Seenu, N., 2004, *ApJ*, 617, 667-679
- Dreicer, H. 1960, *Phys. Rev.*, 117, 329
- Dumont, S., Mouradian, Z., Pecker, J.-C., Vial, J.-C., & Chipman, E., 1982, *Solar Phys.*, 83, 27-50
- Fleishman, G. D., & Melnikov, V. F., 1998, *Phys. Uspekhi*, 41, 1157
- Fleishman, G. D., Gary, D. E., & Nita, G. M., 2003, *ApJ*, 593, 571
- Fleishman, G. D., Nita, G. M., & Gary, D. E., 2005, *ApJ*, 620, 506-516
- Fludra, A., Del Zanna, G., Alexander, D., and Bromage, B. J. I., 1999, *J. Geoph. Res.*, 104, 9709
- Gallagher, P. T., Mathioudakis, M., Keenan, F. P., Phillips, K. J. H., & Tsinganos, K., 1999, *ApJ*, 524, L133-L137
- Gary, G. A., 1989, *ApJSS*, 69, 323-358
- Georgoulis, M. & Vlahos, L., 1998, *A&A*, 336, 721
- Giménez de Castro, C. G., Silva, A. V., Trottet, G., Krucker, S., Costa, J. E., Kaufmann, P., Correia, E., Lüthi, T., Magun, A., Levato, H., 2005, *AIP Conf. Proc.*, 784, 566
- Grigis, P. & Benz, A. O., 2004, *A&A*, 426, 1093-1101
- Güdel, M., Benz, A. O., & Aschwanden, M., 1991, *A&A*, 251, 285
- Gudiksen, B. V., & Nordlund, A., 2002, *ApJ*, 572, L113-L116
- Helander, P., and Sigmar, D., 2002, *Collisional transport in Magnetized Plasmas*, Cambridge Monographs on Plasma Physics, Cambridge Univ. Press
- Karimabadi, Menyuk, C. R., Sprangle, P., & Vlahos, L. 1987, *ApJ*, 316, 462
- Koch, H. W., and Motz, J. W., 1959, *Rev. Mod. Phys.*, 31, 920
- Kotov V. A., Kotov, S. A., & Setyaev, V. V., 2002, *Solar Physics*, 209, 233
- Kuijpers, J., & Slotje, C., 1976, *Solar Phys.*, 46, 247
- Lee, J., and Gary D., E., 2000, *ApJ*, 543, 457
- Lin, R. P., 1998, *Space Science Reviews*, 86, 61-78
- Littlejohn, R. B., 1981, *Phys. Fluids*, 24, 1730
- Littlejohn, R. B., 1983, *J. Plasma Physics*, 29, 111
- Littlejohn, R. B., 1988, *Phys. Rev. A*, 38, 6034
- MacLeod, M. A., 1995, *Inverse Problems*, 11, 1087-1096
- Matthaeus, W. H., & Lamkin, S. L., 1986, *Phy. Fluids*, 29, 2513
- Nita, G. M., Gary, D. E., & Fleishman, G. D., 2005, *ApJ*, 629, L65-L68
- Nobile, A. G., Ricciardi, L. M., & Sacerdote, L., 1985, *J. Appl. Prob.*, 22, 360-369
- Papadopoulos, K. 1980, in: *Dynamics of the Magnetosphere*, ed S.-I. Akasofu (Dordrecht: Reidel)
- Parker, E. N., 1972, *ApJ*174, 499
- Parker, E. N., 1983, *ApJ*264, 635
- Parker, E. N., 1993, *ApJ*, 414, 389-398
- Petrie, G. J. D., & Lothian, R. M., 2003, *A&A*, 398, 287

- Press, W., Teukolsky, S., Vetterling, W., and Flannery, B., 1998, Numerical recipes in C, 2nd ed., Cambridge Univ. Press, Cambridge
- Rantsiou, E., 2004, Reconstruction of coronal force-free magnetic fields with constant α from photospheric observations, *Diploma Thesis*, Aristotle University of Thessaloniki, Greece
- Saint-Hilaire, P., & Benz, A. O., 2003, *Solar Phys.*, 216, 205S
- Schlickeiser, R., 2003, *Springer Lecture Notes on Physics*, 612, 230-260
- Schott, G. A., 1912, *Electromagnetic Radiation*, Cambridge.
- Schumacher, J., & Kliem, B., 1996, *Phys. Plasmas*, 3, 4703
- Spicer, D. S., & Sudan, R. N., 1984, *ApJ*, 280, 448-456
- Török, T., & Kliem, B., 2001, *Proc. 6th Internat. School/Symposium ISSS-6*, ed. J. Büchner, Garching, Germany, p. 364
- Vlahos, L., & Georgoulis, M., 2004, *ApJ*, 603, L61
- Wheatland, M. S., 1999, *ApJ*, 518, 948-953